




## Parameter space mapping of the Princeton magnetorotational instability experiment

Himawan W. Winarto <sup>1</sup>, Hantao Ji <sup>1,2</sup>, Jeremy Goodman,<sup>1</sup> Fatima Ebrahimi,<sup>1,2</sup> Erik P. Gilson,<sup>2</sup> and Yin Wang <sup>2</sup>

<sup>1</sup>*Department of Astrophysical Sciences, Princeton University, Princeton, New Jersey 08544, USA*

<sup>2</sup>*Princeton Plasma Physics Laboratory, Princeton University, Princeton, New Jersey 08543, USA*



(Received 17 April 2020; accepted 20 July 2020; published 24 August 2020)

Extensive simulations of the Princeton Magnetorotational Instability (MRI) Experiment with the Spectral/Finite Element code for Maxwell and Navier-Stokes Equations (SFEMaNS) have been performed to map the MRI-unstable region as a function of inner cylinder angular velocity and applied vertical magnetic field. The angular velocities of the outer cylinder and the end-cap rings follow the inner cylinder in fixed ratios optimized for MRI. We first confirm the exponential growth of the MRI linear phase using idealized conducting vertical boundaries (end caps) rotating differentially with a Taylor-Couette profile. Subsequently, we run a multitude of simulations to scan the experimental parameter space and find that the normalized volume-averaged mean-square radial magnetic field, our main instability indicator, rises significantly where MRI is expected. At various locations, the local radial components of fluid velocity and generated magnetic field are well correlated with the volume-averaged indicator. Based on this correlation, a diagnostic system that will measure the radial magnetic field at several locations on the inner cylinder is proposed as the main comparison between simulation and experiment. A detailed analysis of poloidal mode structures in the SFEMaNS code indicates that MRI, rather than Ekman circulation or Rayleigh instability, dominates the fluid behavior in the region where MRI is expected.

DOI: [10.1103/PhysRevE.102.023113](https://doi.org/10.1103/PhysRevE.102.023113)

### I. INTRODUCTION

The magnetorotational instability (MRI) has been extensively studied as an efficient way to transport angular momentum in accretion disks [1]. While accretion disks are stable to both linear and most likely nonlinear hydrodynamic instability [2,3], the presence of a vertical magnetic field renders the disk susceptible to the so-called standard MRI. As such, MRI is believed to be the main driving mechanism of the turbulence and angular momentum transport in accretion disks. Over the last few decades, investigations of MRI were mostly done through numerical simulations focusing on local phenomena. Using convenient, yet artificial, shearing-box boundary conditions, it is possible to simulate a small portion of an accretion disk and investigate the local angular momentum transport [4]. However, it is not yet possible to obtain such small-scale measurements from astronomical observation. This motivates the need for laboratory experiments, which will verify the existence of simulated MRI behaviors. The possibility of recreating MRI in a laboratory setting is based on the fact that MRI does not depend directly on the flow driving mechanism, but rather on the flow profile of angular velocity versus cylindrical radius,  $\Omega(r)$ , at least in the linear regime. The Princeton MRI experiment is designed to demonstrate the standard MRI in a modified Taylor-Couette device filled with liquid metal [5,6]. Other forms of MRI, the Helical MRI [7] and the Azimuthal MRI [8], have been detected in the laboratory but unfortunately are lacking of clear relevance to Keplerian disks [9].

The Princeton apparatus incorporates several modifications to a typical Taylor-Couette device. Split end caps, functioning as the additional rotational degrees of freedom in the vertical

boundaries, are used to minimize Ekman circulation and better approximate the desired ideal Couette flow profile at the midplane [2,3,10,11]. A split end-cap configuration is also shown to significantly reduce Ekman circulation in similar experiment aimed to investigate Helical MRI [12]. Nevertheless, the difference in angular velocity between end-cap rings drives a shear layer into the fluid interior where the shear parameter  $q$ , defined as

$$q = -\frac{\partial \ln \Omega}{\partial \ln r}, \quad (1)$$

exceeds the critical value of 2. The shear layer occurs both without [13] and with [14] magnetic field corresponding to Stewartson and Stewartson-Shercliff layers, respectively. These layers can be locally unstable to the Rayleigh instability or Kelvin-Helmholtz instability [15]. The end caps are made from copper, and hence are electrically conducting, in order to drive the azimuthal flow more strongly than purely viscous coupling by electrically insulating end caps. They will thereby enhance the saturation amplitude of MRI [16,17]. By capturing the magnetic field lines, the conductivity of the end caps intensifies the Stewartson-Shercliff layer in some flow regimes, but less so in those regimes where MRI is expected, as has been shown both experimentally [17] and numerically [18].

In this paper, we first perform a detailed benchmark study of our numerical framework (SFEMaNS) [19] by demonstrating the exponentially growing behaviors from the linear phase of MRI. For this purpose, we simulate an idealized version of our system with no-slip vertical boundaries that rotate with a continuous ideal Taylor-Couette profile. The growth rates obtained are compared to local WKB

(Wentzel-Kramers-Brillouin) [5] and linear [20] calculations with periodic vertical boundaries. We then realistically model the experimental boundary conditions in order to map the predicted MRI-unstable region through the entire experimental parameter space of inner cylinder angular velocity and applied magnetic field. The other angular velocities are scaled in fixed proportions suitable for MRI. Unlike previous simulations in the MRI regime [16,18], our simulations mimic experimental protocols by first relaxing the hydrodynamic flow before applying the vertical magnetic field. Poloidal magnetic fields and velocities are found to be well correlated in the expected MRI-unstable regime. By analyzing the poloidal structures of magnetic and velocity fields, we then distinguish the effects of Rayleigh instability and Ekman circulation from those of MRI. In addition, a diagnostic system is proposed based on point measurements of the radial magnetic field on the inner cylinder. This quantity is shown to be well correlated with a global average of the magnetic perturbations as an indicator of MRI and is more accessible experimentally.

This paper is organized as follows. Section II describes the simulation model of the experiment and important experimental parameters. Section III maps the MRI-unstable region in our parameter space. The region is mapped by evaluating the volume-averaged root-mean-square radial magnetic field normalized by the imposed axial field (“MRI signal”) [15]. We show that this signal is well correlated with the local radial magnetic field at the surface of the inner cylinder and fluid velocity at the midplane near the inner cylinder. On the basis of this correlation, we propose a diagnostic measure to better bridge the gap between experiment and simulation. Furthermore, we provide physical insights on how to distinguish MRI from secondary effects of Rayleigh instability and Ekman circulation. Finally, Sec. IV summarizes our main results and conclusions.

## II. NUMERICAL SETUP AND SIMULATION BENCHMARK

The Princeton MRI experiment, shown in Fig. 1(a), is a modified Taylor-Couette device comprising two concentric cylinders with inner radius  $R_1 = 7.06$  cm, outer radius  $R_2 = 20.3$  cm, and fluid height  $h = 28$  cm. The top and bottom end caps are divided at  $R_3 = 13.25$  cm into inner and outer rings. The outer rings are currently set to co-rotate with the outer cylinder [17], while the inner rings rotate independently of both cylinders. A recent modification added a 1 cm rim on the inner cylinder to further reduce Ekman circulation [3]. The working fluid is liquid gallium-indium-tin eutectic, known as Galinstan, with composition of Ga:In:Sn = 67:20.5:12.5, density  $\rho_G = 6.36 \times 10^3$  kg/m<sup>3</sup>, conductivity  $\sigma_G = 3.1 \times 10^6$   $\Omega^{-1}\text{m}^{-1}$ , viscosity  $\nu = 2.98 \times 10^{-7}$  m<sup>2</sup>/s, and magnetic diffusivity  $\eta = 2.57 \times 10^{-1}$  m<sup>2</sup>/s.

In order to fully understand and predict the MRI effect amid other competing effects, the experiment is modeled in fully nonlinear simulations. The current simulation model is based on the Spectral/Finite Element code for Maxwell and Navier-Stokes Equations (SFEMaNS) [19]. The finite-element framework of SFEMaNS is well suited to model important fluid-boundary interactions in the experimental device. The code solves the dimensionless Navier-Stokes and induction equations for incompressible flow on a mesh in the

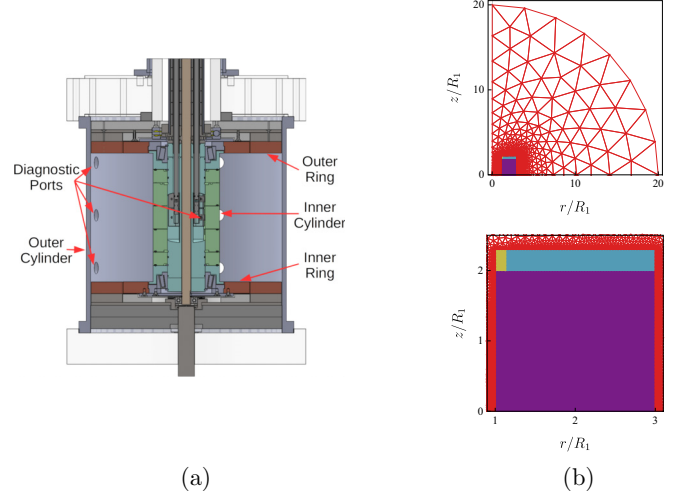


FIG. 1. (a) Cross section of Princeton MRI experiment and (b) its mesh model for SFEMaNS simulations. The fluid domain has a mesh resolution of 100 by 200 triangular cells. A sparse vacuum mesh surrounds the system with radius  $R_{\text{vacuum}} = 20R_1$ . Colors indicate different domains with purple as the fluid, blue as the copper end-cap rings, yellow as stainless steel inner cylinder rim, and red as vacuum.

poloidal  $(r, z)$  plane, divided into fluid, solid, and vacuum domains as shown in Fig. 1(b). The two equations solved for the fluid domain are given by

$$\frac{\partial \vec{u}}{\partial t} + (\vec{\nabla} \times \vec{u}) \times \vec{u} - \text{Re}^{-1} \Delta \vec{u} + \vec{\nabla} p = (\vec{\nabla} \times \vec{H}) \times (\mu_0 \vec{H}), \quad (2)$$

$$\frac{\partial}{\partial t} (\mu_0 \vec{H}) + \vec{\nabla} \times (\text{Rm}^{-1} \sigma^{-1} \vec{\nabla} \times \vec{H}) = \vec{\nabla} \times (\vec{u} \times \mu_0 \vec{H}). \quad (3)$$

Here  $\vec{u}$  is the velocity,  $\vec{H}$  the magnetic field,  $p$  the pressure,  $\mu_0$  the vacuum permeability, and  $\sigma$  is conductivity. The dimensionless Reynolds number and magnetic Reynolds number are denoted by  $\text{Re}$  and  $\text{Rm}$ . In the solid boundaries, only Eq. (3) is solved to describe the evolution of magnetic field. The fluid cavity and end caps are then surrounded by a spherical vacuum region where the magnetic field is represented by a scalar potential satisfying  $\vec{H} = \vec{\nabla} \phi$ . A uniform vertical field, denoted by  $B_z$  unless otherwise stated, is imposed by setting  $\phi = B_z z$  at the outer edge of the vacuum region. While SFEMaNS is capable of fully three-dimensional calculations via a Fourier azimuthal spectral decomposition, the simulations reported here are axisymmetric.

The computation is normalized in the units of the radius  $R_1$  and angular velocity of the inner cylinder  $\Omega_1$  in addition to the density  $\rho_G$  and conductivity  $\sigma_G$  of Galinstan. Important dimensionless parameters of the simulations are the Reynolds number  $\text{Re} \equiv \Omega_1 R_1^2 / \nu$ , magnetic Reynolds number  $\text{Rm} \equiv \Omega_1 R_1^2 / \eta$ , and Lehnert number  $B_0 \equiv B_z / (\Omega_1 R_1 \sqrt{\mu_0 \rho})$ . The mesh is simplified, as shown in Fig. 1(b), with  $R_2 = 3R_1$ ,  $R_3 = 2R_1$ ,  $h = 4R_1$  and inner cylinder rim radius of  $R_{\text{rim}} = 1.15R_1$ . The thickness of the end caps is  $d = 0.3R_1$  and modeled as copper with conductivity  $\sigma_{\text{Cu}} = 6.0 \times 10^7$   $\Omega^{-1}\text{m}^{-1} \approx 19\sigma_G$ . The inner cylinder rim is modeled as stainless steel with conductivity  $\sigma_{\text{SS}} = 1.45 \times 10^6$   $\Omega^{-1}\text{m}^{-1} \approx 0.47\sigma_G$ .

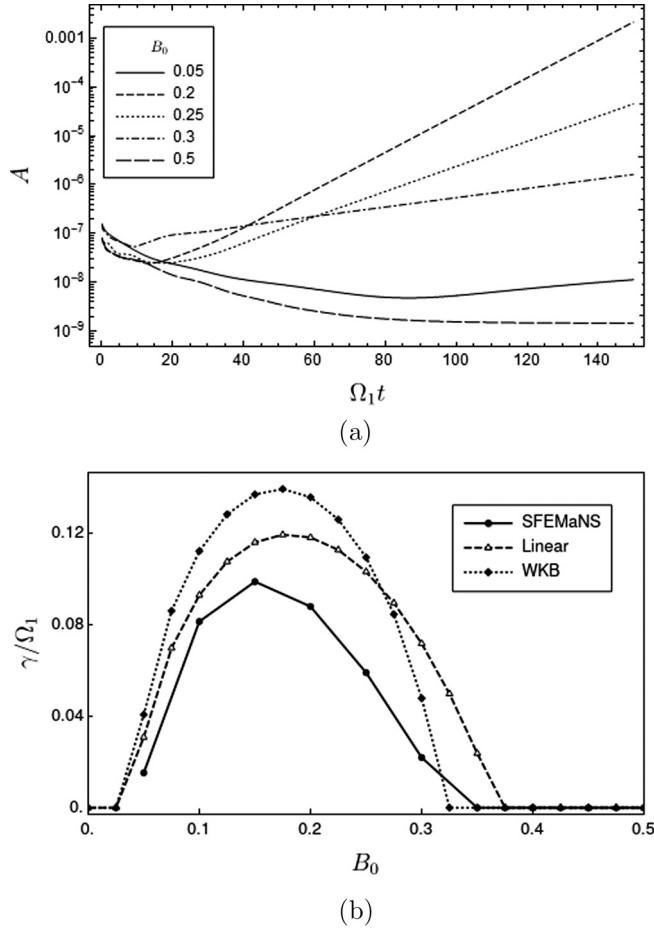


FIG. 2. (a) Evolutions of the MRI signal as a function of time for SFEMaNS simulations with ideal Taylor-Couette end-cap profile at  $\text{Rm} = 20$  with  $\Omega_2/\Omega_1 = 0.1325$ . (b) Growth rate comparison from WKB, linear, and SFEMaNS calculations with the same flow parameters. Growth rates from SFEMaNS simulations are calculated from the last 50  $\Omega_1^{-1}$  of 150  $\Omega_1^{-1}$  runs.

### A. Benchmark of numerical code

To demonstrate the capability of the SFEMaNS code to resolve MRI-related effects, a benchmark study is performed by comparing the SFEMaNS results with WKB [5] and linear eigenmode [20] calculations for the ideal Taylor-Couette profile. For this purpose, the vertical boundaries are modified to rotate with a continuous ideal Taylor-Couette profile  $\Omega(r) = a + br^{-2}$ . The constants  $a$  and  $b$  are chosen to match the radial boundaries with  $\Omega(R_1) = \Omega_1$  and  $\Omega(R_2) = \Omega_2 = 0.1325\Omega_1$ . For the comparison, we use  $\text{Rm} = 20$  and  $\text{Re} = 1000$  and calculate the growth rate from the exponential growth of the MRI signal  $A$  defined as [15]

$$A = \sqrt{\frac{1}{|\nabla_f|} \int_{\nabla_f} \frac{B_r^2}{B_z^2} dV}, \quad (4)$$

with  $B_r$  as the local radial magnetic field is normalized to the externally imposed axial magnetic field  $B_z$  and averaged over the fluid domain  $\nabla_f$ .

Figure 2(a) shows the exponential growth of the MRI signal  $A$  for different values of  $B_0$ , obtained from SFEMaNS

code with the idealized vertical boundaries. At  $\text{Rm} = 20 \ll \text{Re} = 1000$ , there is a MRI-susceptible range of  $B_0$  as shown by the WKB dispersion equation expressed in simulation variables:

$$\left[1 + \frac{k_r^2}{k_z^2}\right][\gamma(\gamma + 1) + S^2]^2 + 2\zeta\widetilde{\text{Rm}}^2(\gamma + 1)^2 - 2(2 - \zeta)\widetilde{\text{Rm}}^2 S^2 = 0. \quad (5)$$

Here  $\gamma$  is the linear MRI growth rate while  $S \equiv k_z B_0 \text{Rm}/k^2$  is the Lundquist number with  $k_z = n_z \pi/h$ ,  $k_r = n_r \pi/(R_2 - 1)$ , and  $k = \sqrt{k_r^2 + k_z^2}$  as the WKB wave numbers. The dimensionless vorticity parameter is  $\zeta = 2(R_2^2 \Omega_2 - 1)/[(R_2^2 - 1)\sqrt{\Omega_2}]$  and the modified magnetic Reynolds number is  $\widetilde{\text{Rm}} \equiv \text{Rm}\sqrt{\Omega_2}/k^2$ . From the symmetry of our device and based on our numerical simulations, we chose  $(n_r, n_z) = (1, 2)$  [16].

The comparison shown in Fig. 2(b) indicates good agreements of the growth rates and the interval in  $B_0$  that is unstable to MRI between modified SFEMaNS simulations, WKB, and linear calculations. Growth rates calculated from SFEMaNS are generally lower than those from WKB and linear calculations. This can be attributed to the difference in vertical boundary conditions. Both WKB and linear calculations are done under the assumption of vertical periodicity, while SFEMaNS simulations are using impenetrable, no-slip, conducting vertical boundaries. This will create dissipative layers, which lower the growth rate by reducing the available free energy in the system. Such layers will also effectively shorten the cylinder height and increase the vertical wave number  $k_z$  increasing magnetic diffusion in the bulk of the fluid. However, the attachment of the field lines to the conducting end caps helps to maintain the unstable flow profile.

### B. Parameter space region of interest

In order to map the MRI-unstable region through the parameter space, we limit our search to the experimentally relevant regime  $\Omega_1 \leq 4000$  rpm and  $B_z \leq 4800$  G. This corresponds to the typical values of  $\text{Re} \sim O(10^7)$ ,  $\text{Rm} \sim O(10)$ , and  $B_0 \sim O(10^{-1})$ . Since such a large  $\text{Re}$  is computationally infeasible, our simulations use  $\text{Re} = 1000$ . While flows with higher  $\text{Re}$  values may have stronger fluctuations, this value of  $\text{Re}$  has been shown previously to suffice for the convergence of the MRI signal to the results of simulations up to  $\text{Re} = 32000$  [16]. Simulations in this paper focus on the MRI configuration for the angular velocity ratios given by  $\Omega_1:\Omega_3:\Omega_2 = 1:0.55:0.1325$ , where  $\Omega_3$  is the angular velocity of the inner rings. This ratio reproduces the ideal Taylor-Couette profile with less than 4% variation on the midplane [21]. The two remaining dimensionless parameters  $\text{Rm}$  and  $B_0$  are varied over their experimentally accessible ranges. To mimic the anatomy of an experimental shot, simulations are done in two steps, in contrast to our previous study [16]. The first stage hydrodynamically relaxes the fluid for 200  $\Omega_1^{-1}$  without magnetic field, starting from an initial piecewise-solid-body condition that follows the end caps' angular velocities. The second stage imposes the vertical magnetic field and continues for another 500  $\Omega_1^{-1}$  to reach approximately steady

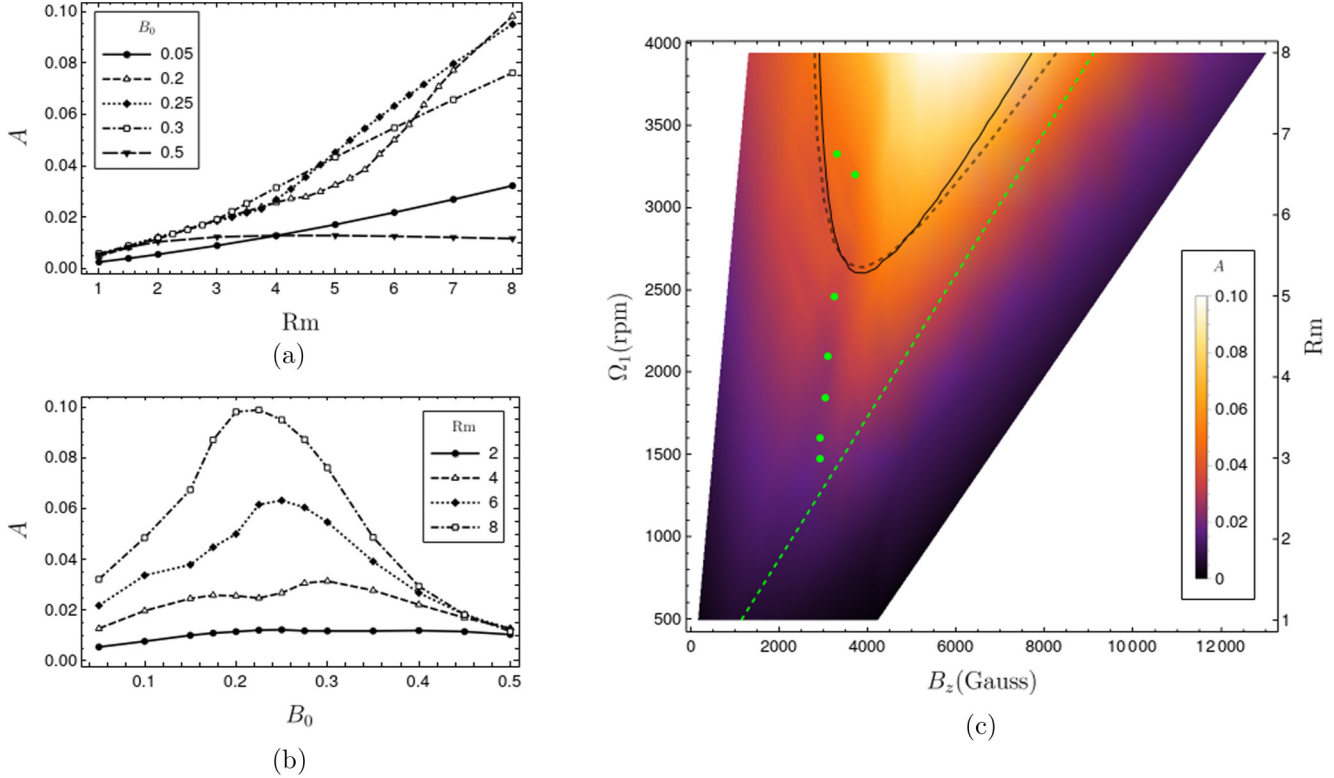


FIG. 3. (a) MRI signal as a function of  $Rm$  and (b)  $B_0$  using the MRI configuration. (c) Contour plot of the MRI signal in the experimental parameter space of external applied magnetic field  $B_z$  and inner cylinder angular velocity  $\Omega_1$ . Green dots indicate the locations of changes in the slope  $(\partial A / \partial Rm)_{B_0}$ . The green dashed line indicates the critical  $B_0 = 0.35$ , which is the smallest Lehnert number without any slope change, indicating the onset of magnetic stabilization. The solid black line indicates the boundary of the MRI-unstable region from the WKB approximation [Eq. (5)], while the dashed black line indicates the boundary from the linear calculation. The MRI signals are averaged over the last 200  $\Omega_1^{-1}$  of each simulation.

states. The flow characteristics reported below come from the last 200  $\Omega_1^{-1}$  of the second phase.

The three main physical quantities monitored in simulations are the MRI signal, the radial velocity near the inner cylinder, and the radial magnetic field on the radial boundaries. The radial fluid velocity on the midplane is directly related to angular-momentum transport and has been extensively studied as an MRI signature in the device [22]. Point measurements of radial magnetic field at discrete locations are investigated in order to validate a diagnostic system using an array of Hall sensors installed on the inner cylinder surface. For each simulation, the MRI signal is monitored every 1  $\Omega_1^{-1}$ , while detailed velocity and magnetic profiles are saved every 10  $\Omega_1^{-1}$ .

### III. RESULTS AND DISCUSSIONS

#### A. The MRI signal

Extensive simulations were performed at constant values of  $B_0$  scanning over the range of  $Rm = 1$  to 8. Constant values of  $B_0$  are represented by lines with different slopes originating from the origin in  $(B_z, \Omega_1)$  parameter space, while  $Rm$  corresponds to  $\Omega_1$ . This scanning method is motivated by the dispersion relation [Eq. (5)], which predicts a limit to  $B_0$  beyond which MRI is suppressed. For a given flow

with ideal Taylor-Couette profile with  $\Omega_2 / \Omega_1 = 0.1325$  and our experimental parameters, the critical  $B_{0,crit}$  is 0.3167. Generally, this critical value depends only on the dimensions of the cylinders and on the ratio of cylinder angular velocities.

Figure 3(a) shows the result of scans for several values of  $B_0$ . In all cases, the MRI signal increases monotonically for  $Rm < 2$ , which can be attributed to the secondary effects of Rayleigh instability and Ekman circulation rather than MRI. At low  $B_0$ , the Lorentz forces are still negligible, even for high  $Rm$  values, and the generated radial magnetic fields are dominated by purely hydrodynamic effects. For simulations with high  $B_0$ , the strength of the MRI signal quickly saturates as we increase  $Rm$ . This is consistent with the expectation that sufficiently strong magnetic fields should stabilize the shear flow [23]. This is more apparent in Fig. 3(b) where the MRI signals decline at  $B_0 \geq 0.3$  for all  $Rm$ .

For intermediate values of  $B_0$ , there exists a slope change in the MRI signal as  $Rm$  increases. This slope change is attributed to the onset of MRI [16]. The locations of these slope changes can be interpreted as the low-field threshold of the MRI-unstable region. Extending the simulations over the entire experimental parameter space, we can plot the contour of the MRI signal as shown in Fig. 3(c). The presence of “knees” in the MRI signal for constant  $B_0$  is observed for multiple values between 0.175 and 0.3. The high limit value of  $B_0$  in simulation is found to be  $B_{0,crit} = 0.35$ , beyond which

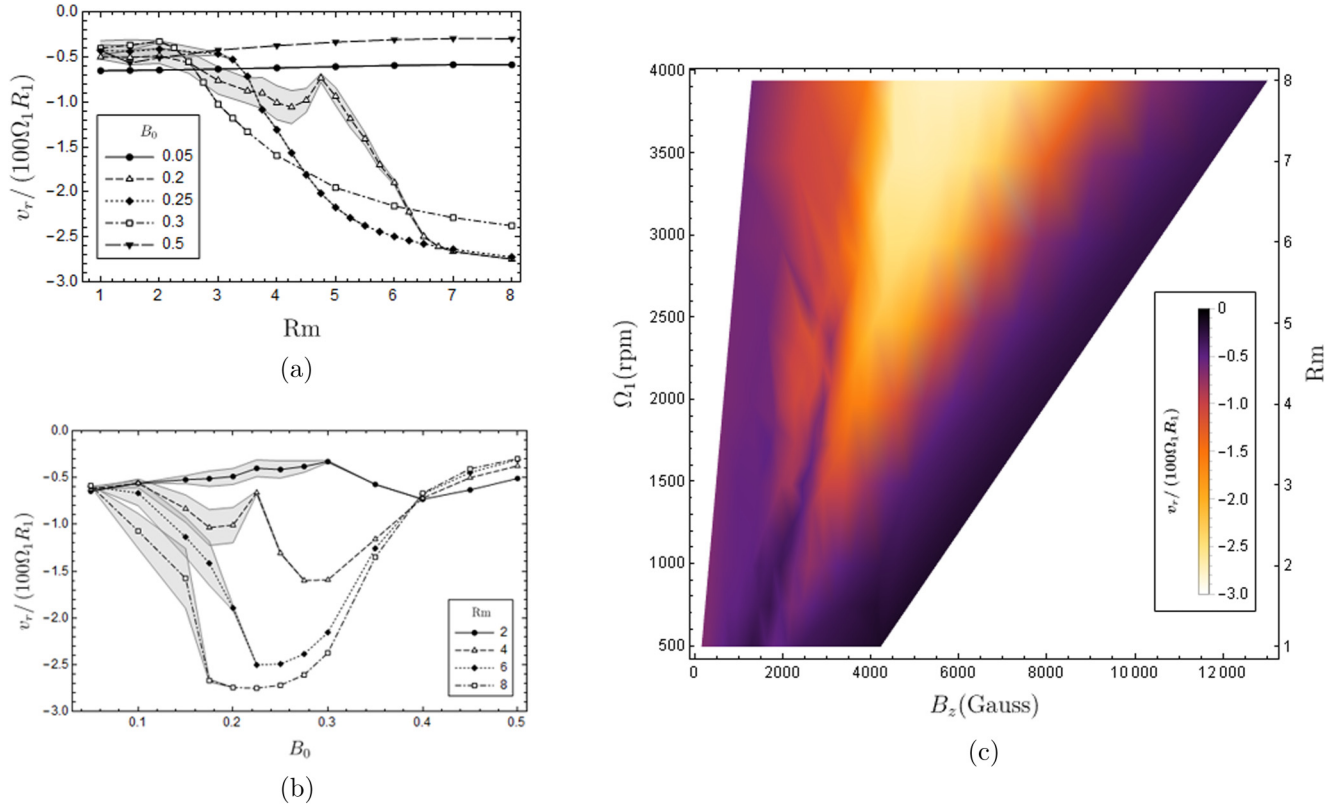


FIG. 4. (a) Radial velocity of fluid element at  $(r, z) = (1.15R_1, 0)$ , or the jet velocity, as a function of  $Rm$  and (b)  $B_0$  using the MRI configuration. Gray shadows around the lines indicate their standard deviation of mean from the averaging process. (c) Contour plot of the jet velocity in the experimental parameter space of external applied magnetic field  $B_z$  and inner cylinder angular velocity  $\Omega_1$ . The jet velocities are averaged for the last 200  $\Omega_1^{-1}$  of each simulation.

the strength of the MRI signal stabilizes at high  $Rm$  values. This limit can be used to set the high field boundary of the MRI-unstable region. It is then possible to qualitatively isolate the MRI-unstable region of the parameter space between the two limits. The resulting region extends beyond the one derived from the linear analysis and includes parameters as low as  $Rm \approx 3$  or  $\Omega_1 \approx 1500$  rpm at  $B_0$  of 0.3. Extension of the MRI-unstable region from the simple WKB and linear predictions is attributed to complex interactions with boundaries and secondary effects that cannot be captured with the simple models.

**B. Radial velocity**

The angular momentum transport effect due to MRI is expected to induce observable radial flows, which correlate to the radial magnetic field and thus the MRI signal. Figure 4 shows plots of the radial fluid velocities at a point with  $r = 1.15R_1$  on the midplane. The radial distance is chosen to be close enough to the inner cylinder yet far away such that it will not be in the inner cylinder boundary layer. The midplane is chosen to utilize the symmetry of the system and to be as far as possible from the vertical boundary layers.

For simulations inferred to be in the MRI-unstable region, based on MRI signal analysis, there are significant increases of the radial velocity at the particular location. The increases are consistent with an earlier numerical study of the device categorizing this as the “jet” velocity due to MRI [22].

In Fig. 4(a) the jet velocities saturate at high  $Rm$  for values of  $B_0$  susceptible to MRI. The saturation value can be attributed to the solid boundaries of the system, which force fluid circulation as the total volume has to be conserved. Translating the results into the parameter space of the experiment, as shown in Fig. 4(c), similar contours to the MRI signal can be found by observing the jet velocity.

In practice, the jet velocity is perhaps directly measurable, whereas the MRI signal is not, as it would require  $B_r$  measurements throughout the fluid volume. While the measurement of the radial velocity from a single location is possible, it is not trivial. The current method to measure the fluid velocity using ultrasound Doppler velocimetry (UDV) [24] can give only the magnitude of fluid velocity along a straight line from the sensor. The measured velocity will generally be dominated by its tangential component coming from the rotating motion. Measurement of the radial vector component will require correlating two ultrasound measurements that intersect at a point. This technique is prone to statistical error due to the typically low signal-to-noise ratio in addition to the oxide build-up in the system that limits the measurement depth.

**C. Point measurements of radial magnetic field on inner cylinder**

Due to the inability to directly measure the volume-averaged MRI signal and the difficulty of measuring the jet velocity, a diagnostic method is suggested to measure the

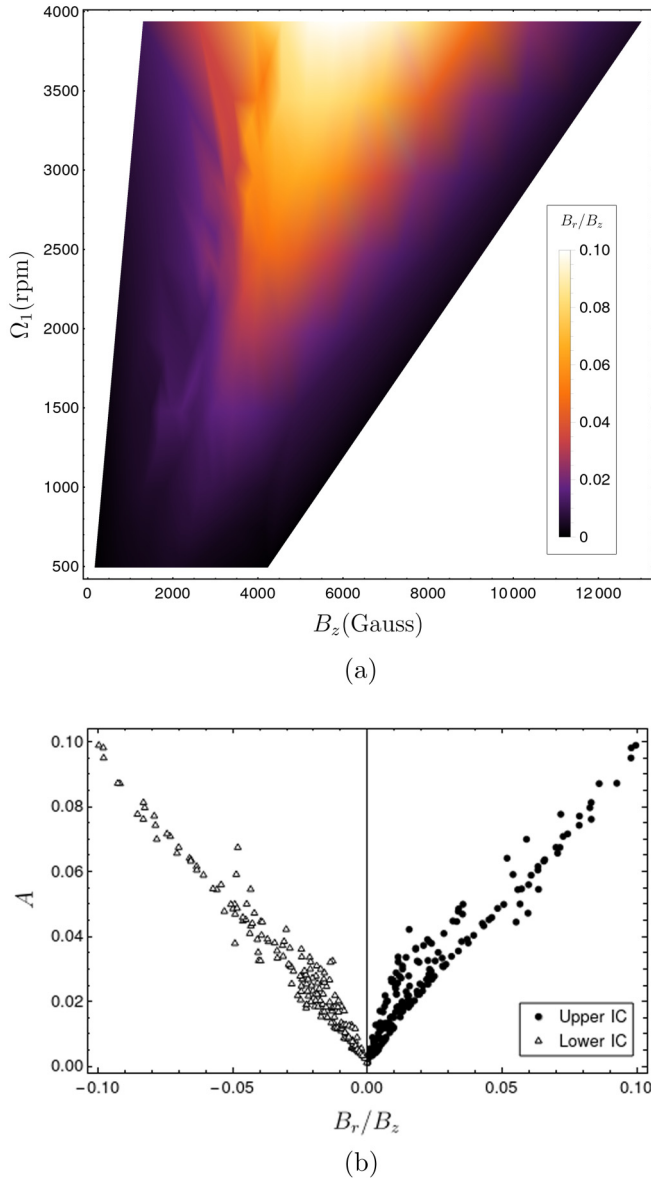


FIG. 5. (a) Contour plot of the normalized point measurement of radial magnetic field in the experimental parameter space measured at  $(r, z) = (R_1, 1.57R_1)$  at the final time steps of simulations. (b) Relation between the value radial magnetic field at  $(r, z) = (R_1, \pm 1.57R_1)$  at the final time steps to their averaged MRI signals from the last  $200 \Omega_1^{-1}$ .

onset of MRI in the system. Our proposed diagnostic system is based on an array of Hall sensors installed on the inner cylinder to provide point measurements of radial magnetic field. The array can provide good statistical measurements of the magnetic field mode structures to be compared with the simulations.

The basis of this diagnostic measurement is the direct correlation between the point measurements of radial magnetic field and the MRI signal. From the simulations, measurements at a vertical distance  $1.57R_1$  above the midplane provide a similar contour to the MRI signal as shown in Fig. 5(a). Furthermore, the values of the MRI signal linearly correlate with the strength of the normalized magnetic field at discrete

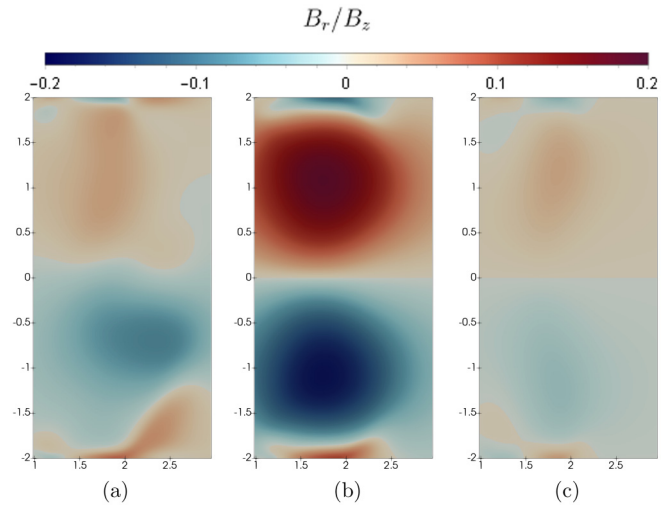


FIG. 6. Poloidal contours of  $B_r/B_0$  for three different values of  $B_0$ : (a) 0.05, (b) 0.25, and (c) 0.5 at  $Rm$  of 8 from their final time steps of simulations. The structures are in steady state for the last  $200 \Omega_1^{-1}$ .

points on the inner cylinder as shown in Fig. 5(b). The change of sign from two measurements at the same distance above and below the midplane comes from the odd vertical mode structure of the radial magnetic field.

#### D. Poloidal structures and the behavior of secondary effects

While the three time-averaged quantities discussed above show similar contours, the contributions of secondary behaviors still need to be investigated to fully isolate the MRI-unstable region. Both Ekman circulation and Rayleigh instability can occur in the system generating both radial magnetic fields and radial fluid motion. It is important to separate and predict the behaviors of secondary effects through detailed examination of the simulated system. As such, we compare the poloidal mode structures of the magnetic and velocity fields in SFEMaNS simulations.

For this purpose, three values of  $B_0$  are chosen for  $Rm$  of 8, which is sufficiently high that all theoretical calculations from WKB, linear, and SFEMaNS predict that there is a closed range of  $B_0$  in which MRI occurs. We focus on the values of  $B_0 = 0.05, 0.25, 0.5$  corresponding to weak, MRI-susceptible, and strong vertical magnetic fields.

##### 1. Radial magnetic field

Plots of the normalized radial magnetic field on the poloidal cross section at the final time step of each simulations are shown in Fig. 6. In all cases, the radial field structures are dominated by the  $k_z = 2\pi/h$  mode. Near the end caps, small enclaves of reversed magnetic field are formed in addition to the magnetized shear layer. In the case of intermediate  $B_0$  values, extensions of this layer to the bulk of the fluid are highly suppressed. After normalization, the induced radial magnetic field is only significant for intermediate values of  $B_0$  and can be directly attributed to MRI. Results from high  $B_0$  in Fig. 6(c) also reinforce this understanding. In the high

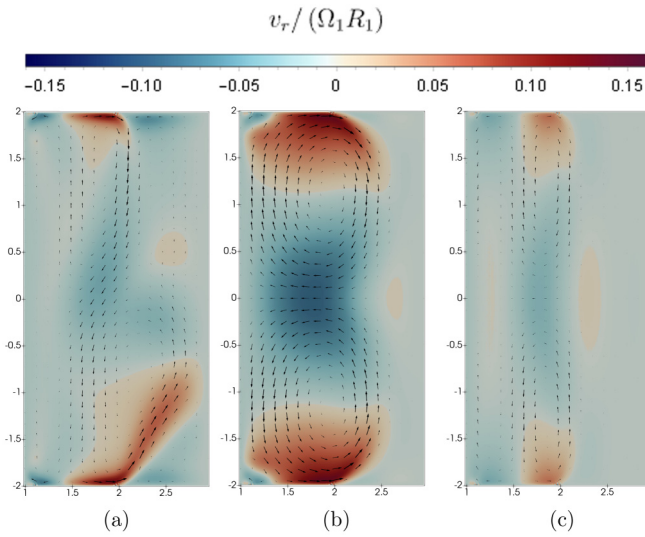


FIG. 7. Poloidal circulation imposed on top of the contour of radial velocity for three different values of  $B_0$ : (a) 0.05, (b) 0.25, and (c) 0.5 at  $Rm$  of 8 from their final time steps of simulations. The structures are in steady state for the last  $200 \Omega_1^{-1}$ .

field setting, MRI should not exist, and the flow should be stabilized, thus the reduction of induced radial magnetic field.

## 2. Poloidal circulation

The onset of Ekman circulation in the system can be determined by comparing the fluid poloidal circulation as shown in Fig. 7. For low  $B_0$  simulations, poloidal fluid movement should be dominated by the Ekman circulation. However, as shown in Fig. 7(a), there is no major poloidal fluid movement occurring in the system with the exception of movement originating from the ring gap of the bottom end cap creating a shear layer. This demonstrates the capability of our end-cap configuration to suppress the Ekman circulation expected in solid end-cap configuration [2,11,25] as well as in a similar end-cap slit configuration [12]. The top-down symmetry breaking may be related to bifurcation phenomena typically observed in short Taylor-Couette flows [11,26]. For an intermediate value of  $B_0$ , suspected to be MRI-unstable, well-defined circulation cells are formed in the system with strong radially inward flow on the midplane. As these cells vanish at low and high vertical fields, they are consistent with the MRI mode that should dominate only at intermediate magnetic field strengths. Such behavior can be attributed to the angular momentum transport from MRI as inward fluid motion is required to transport the angular momentum in the system. The solid boundaries present on the two cylinders force the fluid to change its flow direction. It will then create the two circulation cells instead of a uniform inward motion in fluid domain. In the case of high  $B_0$ , the magnetic field stabilizes the flow profile as shown by the confined shear-layer-induced eddies around the ring gap radius.

## 3. Flow shear

Contours of the flow shear  $q$ , as shown in Fig. 8, are used to analyze the contribution of the Rayleigh centrifugal

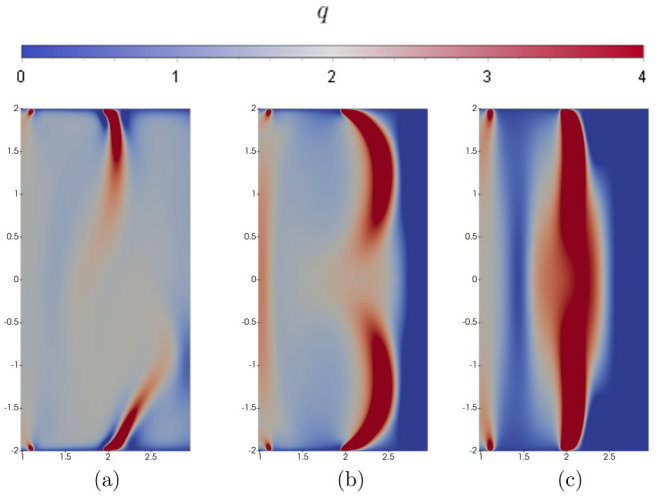


FIG. 8. Poloidal contours of  $q$  for three different values of  $B_0$ : (a) 0.05, (b) 0.25, and (c) 0.5 at  $Rm$  of 8 from the final time steps of the simulations. The structures are in steady state for the last  $200 \Omega_1^{-1}$ . Critical value of Rayleigh instability at  $q = 2$  is denoted by white color. Flow shear of the hydrodynamic cases are nearly identical to the profile in (a).

instability. The Rayleigh instability occurs for flow with  $q > 2$  defined as the high-shear region. This region happens locally in the system, notably around velocity discontinuities at the end caps, consistent with the recent finding on the behavior of magnetized shear layer [17]. In general, this will create a shear layer with effects on the system behavior that can be assumed to be proportional to its volume, as represented by the volume-averaged MRI signal.

In low  $B_0$  simulations, it is apparent that asymmetric shear layers exist and extend to the bulk flow. Due to their proportionally small size, it is unlikely that the system behavior represented by the MRI signal is dominated by the Rayleigh instability in low  $B_0$  simulations. The size of these layers increases with the value of  $B_0$  while becoming symmetric with respect to the midplane as shown in Fig. 8(b). In terms of their fractional volume, the high-shear regions for both intermediate and high valued of  $B_0$  can be considered to be significant corresponding to 34.2% and 32.6% of the total volume. However, in the high- $B_0$  simulation, regions of high  $q$  are confined to the ring-gap radius, while the outer portion of the flow rotates as a solid body. Again, this can be attributed to stabilization of the magnetized shear layer, which reduces the free energy of the system as both the MRI signal and the jet velocity are significantly higher in the case of intermediate  $B_0$ .

Comparing the two cases, the proportion of the high-shear region, which correlates with the extent of Rayleigh instability, should not significantly impact system behavior in the intermediate  $B_0$  case. Furthermore, in this case, the region of high shear coincides with the boundary of circulation cells, which can be attributed to the fluid-boundary interaction. The root-mean-square radial magnetic field of the high-shear region corresponds to 1.19, 1.00, and 1.43 times of the averaged values from the whole region for the low, intermediate, and high  $B_0$  simulations. The lower value in the intermediate  $B_0$

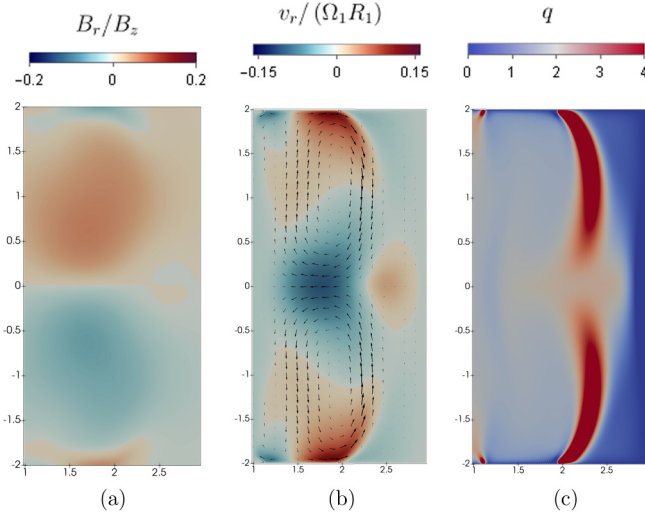


FIG. 9. (a) Poloidal contours of  $B_r/B_0$ , (b) poloidal circulation imposed on top of the contour of radial velocity, and (c) poloidal contours of  $q$  from the final time step of simulation with  $Rm$  of 4 and  $B_0$  of 0.25 in the MRI-unstable region of parameter space. Identical color schemes are used as in the previous comparisons. The three contours indicate similar behaviors to the simulations from the MRI-unstable region at high  $Rm$ .

case supports our understanding that the increase of  $A$  value can be attributed to the existence of a global MRI effect. In the other two cases, the fractional values are significantly higher, yet the corresponding values of  $A$  are much smaller as shown in Fig. 3(b) for  $Rm = 8$ . The size of high-shear regions is approximately constant in the simulation with higher  $Re$  values and slowly decrease as we reduce the  $Re$  value reaching 26.0% of the total volume at  $Re$  of 125.

#### 4. Lower $Rm$ case

The behaviors of MRI-unstable cases are consistent, even in the case of lower  $Rm$  values. Plots of radial magnetic and velocity fields as well as the  $q$ -profile for  $Rm = 4$  with  $B_0 = 0.25$  are shown in Fig. 9. At these parameter values, the system is inside our predicted MRI-unstable region based on the analysis of the MRI signal and jet velocity. While the strength of the induced radial magnetic field is relatively weaker than the case at  $Rm = 8$  with  $B_0 = 0.25$ , it still exhibits a similar structure that is well defined and confined to the two circulation vortices. The system also exhibits strong poloidal circulation similar to the case of higher  $Rm$  that is susceptible to MRI. All of these poloidal structures are consistent with our hypothesis about the MRI behavior. Similarly, the region of high  $q$  is consistently aligned with the boundary of our circulation. The high-shear region covers 25.9% of the total volume and has 0.97 times the root-mean-squared radial magnetic field of the globally averaged value. As the later value is slightly lower than unity, it indicates the existence of dominating global MRI effect in the system.

## IV. CONCLUSION

Full characterization of the MRI-unstable region in the parameter space of the Princeton MRI experiment using SFEMaNS numerical simulations has been presented in this paper. From the observation of the MRI signal, it is possible to estimate the boundaries of the MRI-unstable region. The region is found to extend to lower values of  $\Omega_1$  than predicted by the WKB or linear calculations. This boundary is more experimentally accessible and within the current capability of the experiment. The current experimental campaign at  $Rm = 4$  is close to the lower boundary of the MRI-unstable region.

Effects of MRI in the system can be readily verified by experimentally accessible variables such as the fluid jet velocity and point measurements of radial magnetic field. While both of them are directly correlated with the MRI signal, point measurements of radial magnetic field on the inner cylinder will be used as the basis of a diagnostic system based on Hall sensors due to their simplicity and ease of implementation. The radial magnetic field and radial velocity correspond to the Maxwell and Reynolds stress tensors, respectively, which are commonly used in numerical studies of MRI to quantify angular momentum transport.

Confirmation of the MRI-unstable region can be obtained from the comparison of detailed behaviors from simulations with low, intermediate (MRI-unstable) and high values of external magnetic field at the same angular velocity. In order to isolate MRI behavior from the secondary effects of Ekman circulation and Rayleigh centrifugal instability, detailed poloidal analysis of the radial magnetic field, fluid flow profile, and the shear profile of the flow have been presented. Substantial radial magnetic perturbations and large circulation cells can be observed only for intermediate values of the imposed magnetic field, which confirms the standard behavior of MRI. The simulations demonstrate that Ekman circulation is highly suppressed by the end-cap configuration in simulations. While there are regions with high-flow shear values, the effect of Rayleigh instability remains small with MRI dominating the behavior of simulation in the MRI-unstable region.

Future studies will include secondary effects due to 3D structures of the flow profile. It is also possible to further optimize the MRI-unstable region by varying ratios of  $\Omega_3/\Omega_1$  and  $\Omega_2/\Omega_1$  at the cost of significant increase in computation time. We note that as the ratio  $\Omega_2/\Omega_1$  increases, the average  $q$  value in the system decrease pushing the MRI-unstable region further upwards in the parameter space while decreasing the possibility of Rayleigh instability.

Digital data associated with this work are available from DataSpace at Princeton University [27].

## ACKNOWLEDGMENTS

Prof. Guermond provided the SFEMaNS code used extensively in this paper. This research was supported by DoE (Grant No. DE-AC0209CH11466), NASA (Grant No. NNH15AB25I), NSF (Grant No. AST1312463), and the Max-Planck-Princeton Center for Plasma Physics (MPPC).



- [1] S. Balbus and J. Hawley, *Astrophys. J.* **376**, 214 (1991).
- [2] H. Ji, M. Burin, E. Schartman, and J. Goodman, *Nature (London)* **444**, 343 (2006).
- [3] E. M. Edlund and H. Ji, *Phys. Rev. E* **89**, 021004(R) (2014).
- [4] J. F. Hawley, C. F. Gammie, and S. A. Balbus, *Astrophys. J.* **440**, 742 (1995).
- [5] H. Ji, J. Goodman, and A. Kageyama, *Mon. Not. Astron. Soc.* **325**, L1 (2001).
- [6] H. Ji and S. Balbus, *Phys. Today* **66**(8), 27 (2013).
- [7] F. Stefani, T. Gundrum, G. Gerbeth, G. Rüdiger, M. Schultz, J. Szklarski, and R. Hollerbach, *Phys. Rev. Lett.* **97**, 184502 (2006).
- [8] M. Seilmayer, V. Galindo, G. Gerbeth, T. Gundrum, F. Stefani, M. Gellert, G. Rüdiger, M. Schultz, and R. Hollerbach, *Phys. Rev. Lett.* **113**, 024505 (2014).
- [9] W. Liu, J. Goodman, I. Herron, and H. Ji, *Phys. Rev. E* **74**, 056302 (2006).
- [10] A. Kageyama, H. Ji, J. Goodman, F. Chen, and E. Shoshan, *J. Phys. Soc. Jpn* **73**, 2424 (2004).
- [11] E. Schartman, H. Ji, M. Burin, and J. Goodman, *Astron. Astrophys.* **543**, A94 (2012).
- [12] F. Stefani, G. Gerbeth, T. Gundrum, R. Hollerbach, J. Priede, G. Rüdiger, and J. Szklarski, *Phys. Rev. E* **80**, 066303 (2009).
- [13] E. J. Spence, A. H. Roach, E. M. Edlund, P. Sloboda, and H. Ji, *Phys. Plasmas* **19**, 056502 (2012).
- [14] A. H. Roach, E. J. Spence, C. Gissinger, E. M. Edlund, P. Sloboda, J. Goodman, and H. Ji, *Phys. Rev. Lett.* **108**, 154502 (2012).
- [15] C. Gissinger, J. Goodman, and H. Ji, *Phys. Fluids* **24**, 074109 (2012).
- [16] X. Wei, H. Ji, J. Goodman, F. Ebrahimi, E. Gilson, F. Jenko, and K. Lackner, *Phys. Rev. E* **94**, 063107 (2016).
- [17] K. J. Caspary, D. Choi, F. Ebrahimi, E. P. Gilson, J. Goodman, and H. Ji, *Phys. Rev. E* **97**, 063110 (2018).
- [18] D. Choi, F. Ebrahimi, K. J. Caspary, E. P. Gilson, J. Goodman, and H. Ji, *Phys. Rev. E* **100**, 033116 (2019).
- [19] J.-L. Guermond, R. Laguerre, J. Léorat, and C. Nore, *J. Comp. Phys.* **228**, 2739 (2009).
- [20] J. Goodman and H. Ji, *J. Fluid Mech.* **462**, 365 (2002).
- [21] A. Roach, Ph.D. thesis, Princeton University, 2013.
- [22] W. Liu, J. Goodman, and H. Ji, *Astrophys. J.* **643**, 306 (2006).
- [23] S. Chandrasekhar, *Hydrodynamic and Hydromagnetic Stability*. (Oxford University Press, Oxford, 1961).
- [24] Y. Takeda, *Exp. Therm. Fluid Sci.* **10**, 444 (1995).
- [25] A. V. Obabko, F. Cattaneo, and P. F. Fischer, *Phys. Scr.* **2008**, 014029 (2008).
- [26] G. Pfister, H. Schmidt, K. Cliffe, and T. Mullin, *J. Fluid Mech.* **191**, 1 (1988).
- [27] <http://arks.princeton.edu/ark:/88435/dsp01x920g025r>.